Resonant Inelastic X-Ray Scattering and Non Resonant X-ray Emission Spectra from Coupled-Cluster (Damped) Response Theory

Rasmus Faber* and Sonia Coriani*

Department of Chemistry, Technical University of Denmark,

Kemitorvet Building 207, 2800 Kongens Lyngby, Denmark

E-mail: rfaber@kemi.dtu.dk; soco@kemi.dtu.dk

October 10, 2018

Abstract

A coupled cluster protocol rooted in damped response theory is presented for computing Resonant Inelastic X-Ray Scattering spectra of molecules in gas-phase. Working equations are reported for both linear (i.e., equation-of-motion) and non-linear parametrizations of the coupled-cluster wavefunction response. A simple scheme to compute non-resonant X-ray emission spectra is also proposed. Illustrative results are presented for water.

1 Introduction

Resonant Inelastic X-ray Scattering (RIXS), an X-ray analog to resonance Raman spectroscopy, is one of the (high resolution) spectroscopic techniques exploiting X-ray radiation that has gained increasing popularity in recent years in parallel with the advancements in X-ray radiation sources and facilities, in particular synchrotrons.

RIXS combines X-ray absorption (XAS) with X-ray emission (XES); it can be viewed as a two-photon process that starts with the excitation of a core electron into a valence orbital, as in XAS, followed by detection of a photon emitted by the decay of an electron from a different orbital when filling the core hole, as in XES.[1,2] Thus, while XAS provides information about the unfilled density of states, RIXS probes the electronic structure of the filled density of states.

RIXS data are often reported as two-dimensional plots, where, for instance, the incident energy is on the x-axis and the (incident − emitted) energy transfer is on the y-axis,[3] or where the incident light/excitation energy is on the y axis and the emission energy is on the x axis.[4] The higher dimensionality of the RIXS data gives more information than standard XAS experiments. RIXS experiments can be performed in a variety of ways on a variety of samples. For example, in the soft X-ray regime (0.1–2 keV), RIXS has been performed on the C, N, and O K-edges in small molecules,[2,4–7] metal oxides,[8] and coordination compounds.[3,9]

As for other X-ray spectroscopies, the interpretation of the RIXS spectra is facilitated by *ab initio* computations of the spectroscopic observables, i.e., in the specific case, calculations of the RIXS cross-sections based on the Kramers-Heisenberg-Dirac (KHD) formula.[1,10] However, as pointed out for instance by Rehn and coworkers,[11,12] the KHD sum-over-states (SOS) expression[10] may converge slowly and require a large number of terms in order to span the spectral range of valence and core-excited states. One may therefore argue that the accuracy of computational methods that only include a few selected channels is only qualitative.

Recently, Rehn et al.[12] have proposed a resonance convergent approach to RIXS cross sections based on the algebraic diagrammatic construction (ADC)[13] of the polarization propagator in its so-called intermediate state representation (ISR) variant.[14,15] Inspired by the work of Rehn et al.,[12] we present here a coupled cluster methodology to compute RIXS amplitudes and cross sections of medium-sized molecules based on (damped) response theory[16,17] and equation-of-motion (EOM)[18–20] coupled cluster at the coupled-cluster singles

and doubles level (CCSD). To the best of our knowledge, this is the first time that coupled cluster methods are extended to the computation of RIXS spectra.

A simple scheme to compute non-resonant X-ray emission spectra is also proposed, that does not require unrestricted Hartree-Fock calculations of the neutral species and the cations.

Illustrative results are reported for the water molecule in gas-phase, which allows us to directly compare with the results obtained at the ADC level by Rehn et al.[12] and with existing experimental data.

2 Theory

2.1 The KHD scattering amplitudes in CC and EOM-CC response theory

According to time-dependent perturbation theory, the (right) KHD scattering amplitudes can be written as[10,12]

$$\mathcal{F}^{f0}_{XY}(\omega) = \sum_n \left[\frac{\left\langle \Psi_f \middle| \hat{X} \middle| \Psi_n \right\rangle \left\langle \Psi_n \middle| \hat{Y} \middle| \Psi_0 \right\rangle}{\omega_n - (\omega + i\gamma_n)} + \frac{\left\langle \Psi_f \middle| \hat{Y} \middle| \Psi_n \right\rangle \left\langle \Psi_n \middle| \hat{X} \middle| \Psi_0 \right\rangle}{\omega_n + (\omega' + i\gamma_n)} \right] , \tag{1}$$

where ω is the frequency of the incident beam, ω' that of the emitted one, and the inverse lifetime parameters of the excited states γ_n have been introduced in a phenomenological way.[21–23] As commonly done in damped response theory,[24–27] one can simplify the above expression by assuming that all excited states have the same inverse lifetime γ, so that the KHD right amplitudes reads

$$\begin{aligned} \mathcal{F}^{f0}_{XY}(\omega) &= \sum_n \left[\frac{\left\langle \Psi_f \middle| \hat{X} \middle| \Psi_n \right\rangle \left\langle \Psi_n \middle| \hat{Y} \middle| \Psi_0 \right\rangle}{\omega_n - (\omega + i\gamma)} + \frac{\left\langle \Psi_f \middle| \hat{Y} \middle| \Psi_n \right\rangle \left\langle \Psi_n \middle| \hat{X} \middle| \Psi_0 \right\rangle}{\omega_n + (\omega' + i\gamma)} \right] \\ &= \sum_{n>0} \left[\frac{\left\langle \Psi_f \middle| \hat{\overline{X}} \middle| \Psi_n \right\rangle \left\langle \Psi_n \middle| \hat{Y} \middle| \Psi_0 \right\rangle}{\omega_n - (\omega + i\gamma)} + \frac{\left\langle \Psi_f \middle| \hat{\overline{Y}} \middle| \Psi_n \right\rangle \left\langle \Psi_n \middle| \hat{X} \middle| \Psi_0 \right\rangle}{\omega_n + (\omega' + i\gamma)} \right] \end{aligned} \tag{2}$$

with e.g. $\hat{\overline{X}} = \hat{X} - \left\langle \Psi_0 \middle| \hat{X} \middle| \Psi_0 \right\rangle$. If $\gamma = 0$, Eq. (2) is identical to the conventional expression for the two-photon transition matrix element between state $|\Psi_0\rangle$ and $|\Psi_f\rangle$, subject to the resonant condition $\omega - \omega' = \omega_f$.[28,29] The latter has been shown long ago[30] to be obtainable as residue of a quadratic response function, and several implementations within different wavefunction/density functional frameworks have appeared over the last three decades.[31] The KHD scattering amplitude given above can then be regarded as a two-photon transition matrix element where a complex damping factor is added to the frequencies ω and ω' as to maintain the same resonant condition – in other words, assuming a Y field oscillating with frequency $\omega + i\gamma$ and a second field, X, oscillating with frequency $(-\omega' - i\gamma)$, subject to the resonant condition $(\omega + i\gamma) + (-\omega' - i\gamma) = \omega - \omega' = \omega_f$.

By analogy, we derive the KHD right scattering amplitude by heuristically introducing a damping term in the CC expression for a two-photon (right) transition moment[17]

$$ {}^{\mathrm{CC}}\mathcal{F}^{f0}_{XY}(\omega) = -L_f\Big(\mathbf{A}^X t^Y(\omega + i\gamma) + \mathbf{A}^Y t^X(-\omega' - i\gamma) + \mathbf{B} t^Y(\omega + i\gamma) t^X(-\omega' - i\gamma)\Big) \tag{3} $$

where L_f indicates the left excitation vector. The latter is, like its right counterpart R_f, obtained solving the CC eigenvalue equations

$$ L_f \mathbf{A} = \omega_f L_f; \quad \mathbf{A} R_f = \omega_f R_f \tag{4} $$

under the biorthogonality condition $L_j R_k = \delta_{jk}$. The Jacobian matrix $\mathbf{A}$ is defined as[16,17]

$$ A_{\mu\nu} = \langle \mu | \exp(-T)[\hat{H}, \tau_\nu] \exp(T) | \mathrm{HF} \rangle \equiv \langle \mu | [\hat{H}^T, \tau_\nu] | \mathrm{HF} \rangle \tag{5} $$

the $\mathbf{B}$ matrix is given by

$$ B_{\mu\nu\rho} = \langle \mu | \exp(-T)[[\hat{H}, \tau_\nu], \tau_\rho] \exp(T) | \mathrm{HF} \rangle \equiv \langle \mu | [[\hat{H}^T, \tau_\nu], \tau_\rho] | \mathrm{HF} \rangle \tag{6} $$

and the property Jacobian $\mathbf{A}^Y$ (for operator $\hat{Y}$) is defined as

$$A^Y_{\mu\nu} = \langle\mu|\exp(-T)[\hat{Y},\tau_\nu]\exp(T)|\mathrm{HF}\rangle \equiv \langle\mu|[\hat{Y}^T,\tau_\nu]|\mathrm{HF}\rangle \tag{7}$$

with $\hat{Y}^T = \exp(-T)\hat{Y}\exp(T)$. We refer to Refs. 16,17 for the definition of the remaining terms. The complex response amplitudes, $t^Y(\omega+i\gamma)$, are found solving[32]

$$\left[\mathbf{A} - (\omega+i\gamma)\mathbf{I}\right] t^Y(\omega+i\gamma) = -\xi^Y \tag{8}$$

with (generally complex) right-hand-side

$$\xi^Y_\mu = \langle\mu|\exp(-T)\hat{Y}\exp(T)|\mathrm{HF}\rangle \equiv \langle\mu|\hat{Y}^T|\mathrm{HF}\rangle \quad . \tag{9}$$

We will return on the solution of Eq. (8) in section 2.3.

In exact theory, the left transition moment is simply the complex conjugate of the right, i.e.

$$\begin{aligned}\mathcal{F}^{0f}_{XY}(\omega) =& \mathcal{F}^{f0}_{XY}(\omega)^* \\ =& \sum_n \left[\frac{\left\langle\Psi_0\middle|\hat{Y}\middle|\Psi_n\right\rangle\left\langle\Psi_n\middle|\hat{X}\middle|\Psi_f\right\rangle}{\omega_n-(\omega-i\gamma)} + \frac{\left\langle\Psi_0\middle|\hat{X}\middle|\Psi_n\right\rangle\left\langle\Psi_n\middle|\hat{Y}\middle|\Psi_f\right\rangle}{\omega_n+(\omega'-i\gamma)}\right].\end{aligned} \tag{10}$$

In CC theory, the left and right transition moments are different, but we can again take inspiration from the above equation and compute the left transition moment generalizing the two-photon left transition moment of CC response theory[17]

$$\begin{aligned}{}^{\mathrm{CC}}\mathcal{F}^{0f}_{XY}(\omega) = -\Big(&\bar{t}^X(\omega'-i\gamma)\left[\mathbf{A}^Y + \mathbf{B}t^Y(-\omega+i\gamma)\right] + \bar{t}^Y(-\omega+i\gamma)\left[\mathbf{A}^X + \mathbf{B}t^X(\omega'-i\gamma)\right] \\ &+\mathbf{F}^X t^Y(-\omega+i\gamma) + \mathbf{F}^Y t^X(\omega'-i\gamma) + \mathbf{G}t^X(\omega'-i\gamma)t^Y(-\omega+i\gamma)\Big)R_f \\ &-\bar{M}_f(\omega_f)\Big(\mathbf{A}^X t^Y(-\omega+i\gamma) + \mathbf{A}^Y t^X(\omega'-i\gamma) + \mathbf{B}t^Y(-\omega+i\gamma)t^X(\omega'-i\gamma)\Big)\end{aligned} \tag{11}$$

The response matrix $\mathbf{F}^X$ is, as usual,[17]

$$F^X_{\mu\nu} = \langle\Lambda|[[\hat{X},\tau_\mu],\tau_\nu]\exp(T)|\mathrm{HF}\rangle \equiv (\langle\mathrm{HF}| + \langle\bar{t}|)[[\hat{X}^T,\tau_\mu],\tau_\nu]|\mathrm{HF}\rangle \ , \tag{12}$$

with $\langle\Lambda| = \langle\mathrm{HF}| + \sum_\lambda \bar{t}_\lambda\langle\lambda|\exp(-T) \equiv (\langle\mathrm{HF}| + \langle\bar{t}|)\exp(-T)$. The auxiliary excited-state multipliers are obtained solving

$$\bar{M}^f\left(\mathbf{A} + \omega_f\mathbf{I}\right) = -\mathbf{F}R_f \ \ , \tag{13}$$

where

$$F_{\mu\nu} = \langle\Lambda|[\hat{H},\tau_\mu],\tau_\nu]\exp(T)|\mathrm{HF}\rangle \equiv (\langle\mathrm{HF}| + \langle\bar{t}|)|[[\hat{H}^T,\tau_\mu],\tau_\nu]|\mathrm{HF}\rangle \tag{14}$$

The complex response multipliers $\bar{t}^X(\omega' - i\gamma)$ are obtained solving

$$\bar{t}^X(\omega' - i\gamma)\left(\mathbf{A} + (\omega' - i\gamma)\mathbf{I}\right) = -\eta^X - \mathbf{F}t^X(\omega' - i\gamma). \tag{15}$$

with

$$\eta^X_\mu = \left\langle\Lambda\middle|[\hat{X},\tau_\mu]\middle|\mathrm{CC}\right\rangle \equiv (\langle\mathrm{HF}| + \langle\bar{t}|)[\hat{X}^T,\tau_\mu]|\mathrm{HF}\rangle \tag{16}$$

Equation (15) is slightly more complicated than Equation (8) as the second term on the RHS is complex for $\gamma \neq 0$, even when $\hat{X}$ is purely real or imaginary.

In the EOM-CC (time-independent) framework, which has been shown to be equivalent to the time-dependent CC-CI parametrization,[33] the first-order amplitudes $t^Y(\omega + i\gamma)$, as well as the right R_f and left L_f excitation vectors, are the same as obtained from CC linear response (CC-LR). The EOM-CC left response vectors, on the other hand, are different from the CC-LR ones, because of the different right-hand-sides η^X and the lack of the $\mathbf{F}$ term[17,33,34]

$${}^{\mathrm{EOM}}\bar{t}^X(\omega' - i\gamma)\left(\mathbf{A} + (\omega' - i\gamma)\mathbf{I}\right) = -{}^{\mathrm{EOM}}\eta^X \tag{17}$$

with

$$
\begin{aligned}
{}^{\mathrm{EOM}}\eta^X_\nu &= \langle\Lambda|\hat{X}\exp(T)|\nu\rangle - \bar{t}_\nu\langle\hat{X}\rangle_{\mathrm{CC}} = (\langle\mathrm{HF}| + \sum_\mu \bar{t}_\mu\langle\mu|)\hat{X}^T|\nu\rangle - \bar{t}_\nu\langle\hat{X}\rangle_{\mathrm{CC}} \\
&\equiv \eta^X_\nu + \sum_{\mu>\nu}\bar{t}_\mu\langle\mu|\tau_\nu\hat{X}^T|\mathrm{HF}\rangle - (\bar{t}\cdot\xi^X)\bar{t}_\nu
\end{aligned}
\tag{18}
$$

where we have highlighted that the EOM-CC η^X vector can be easily obtained from the CC-RSP one with small modifications.

The final EOM expressions for the left and right transition moments are different from the CC-RSP case. The EOM-CC right transition moment takes the form

$$
\begin{aligned}
{}^{\mathrm{EOM-CC}}\mathcal{F}^{f0}_{XY}(\omega) = -L_f\Big[&{}^{\mathrm{EOM}}\mathbf{A}^X t^Y(\omega+i\gamma) + {}^{\mathrm{EOM}}\mathbf{A}^Y t^X(-\omega'-i\gamma) \\
&- (\bar{t}\cdot\xi^X)t^Y(\omega+i\gamma) - (\bar{t}\cdot\xi^Y)t^X(-\omega'-i\gamma) \\
&- (\bar{t}\cdot t^Y(\omega+i\gamma))\xi^X - (\bar{t}\cdot t^X(-\omega'-i\gamma))\xi^Y\Big]
\end{aligned}
\tag{19}
$$

where the EOM-CC property Jacobian is

$$
\begin{aligned}
{}^{\mathrm{EOM}}A^X_{\mu\nu} &= \langle\mu|\hat{X}^T|\nu\rangle - \delta_{\mu\nu}\langle\mathrm{HF}|\hat{X}^T|\mathrm{HF}\rangle \\
&= A^X_{\mu\nu} + \langle\mu|\tau_\nu\hat{X}^T|\mathrm{HF}\rangle(1-\delta_{\mu\nu}) \quad .
\end{aligned}
\tag{20}
$$

The EOM-CC left transition moment takes the form

$$
\begin{aligned}
{}^{\mathrm{EOM-CC}}\mathcal{F}^{0f}_{XY}(\omega) = -\Big[&{}^{\mathrm{EOM}}\bar{t}^X(\omega'-i\gamma)^{\mathrm{EOM}}\mathbf{A}^Y + {}^{\mathrm{EOM}}\bar{t}^Y(-\omega+i\gamma)^{\mathrm{EOM}}\mathbf{A}^X \\
&- (\bar{t}\cdot\xi^X)^{\mathrm{EOM}}\bar{t}^Y(-\omega+i\gamma) - (\bar{t}\cdot\xi^Y)^{\mathrm{EOM}}\bar{t}^X(\omega'-i\gamma)\Big]R_f \\
&+ (\bar{t}\cdot R_f)\left[{}^{\mathrm{EOM}}\bar{t}^Y(-\omega+i\gamma)\cdot\xi^X + {}^{\mathrm{EOM}}\bar{t}^X(\omega'-i\gamma)\cdot\xi^Y\right]
\end{aligned}
\tag{21}
$$

Finally, we remind the reader that the usual complications arising from the non-variational nature of CC theory apply for both CC and EOM-CC, i.e., the left and right transition moments are not well defined individually, only their products (i.e., the transition strengths)

are,[17] and the scattering amplitude must be symmetrized

$$\mathcal{F}^{0f}_{XY}(\omega)\mathcal{F}^{f0}_{ZU}(\omega) = \tfrac{1}{2}{}^{\mathrm{CC}}\mathcal{F}^{0f}_{XY}(\omega){}^{\mathrm{CC}}\mathcal{F}^{f0}_{ZU}(\omega) + \tfrac{1}{2}\left({}^{\mathrm{CC}}\mathcal{F}^{0f}_{ZU}(\omega){}^{\mathrm{CC}}\mathcal{F}^{f0}_{XY}(\omega)\right)^{*} \tag{22}$$

For molecules in the gas-phase (or, in general, isotropic samples) the final scattering cross section is proportional to the transition strengths σ^{0f} averaged over all molecular orientations and over the polarization of the emitted radiation. The latter depends on the angle θ between the polarization vector of the incident photon, and the propagation vector of the scattered one[12]

$$\begin{aligned}\sigma^{0f}_{\theta} =& \frac{\omega'}{\omega}\frac{1}{15}\sum_{XY}\left[\left(2-\frac{1}{2}\sin^2\theta\right)\mathcal{F}^{0f}_{XY}(\omega)\mathcal{F}^{f0}_{XY}(\omega)\right.\\ &\left.+\left(\frac{3}{4}\sin^2\theta-\frac{1}{2}\right)\left(\mathcal{F}^{0f}_{XY}(\omega)\mathcal{F}^{f0}_{YX}(\omega)+\mathcal{F}^{0f}_{XX}(\omega)\mathcal{F}^{f0}_{YY}(\omega)\right)\right]\end{aligned} \tag{23}$$

Eq. 23 will be used in the following sections when computing the RIXS spectral slices.

2.2 The non-resonant emission spectra

Non-resonant XES can be viewed as a two-step process where a core electron is initially ejected by a beam with energy well beyond a given edge ionization potential, followed by relaxation of a valence electron into the core hole with corresponding emission of photon energy. One established method to compute EOM-CCSD XES[35] consists in performing an unrestricted Hartree–Fock (UHF) on the neutral molecule in order to generate a set of molecular orbitals for a subsequent UHF calculation in which a core–hole is introduced and invoking the maximum overlap method (MOM) procedure[36] to prevent the variational collapse of the core–hole. Once this calculation is converged, regular CCSD and EOM-CCSD calculations are carried out, and the relevant emission energies appear as negative eigenvalues. Intensities for the transitions are computed using a similar procedure but with single excitation configuration interaction (CIS) calculations applied to the UHF core–hole wavefunction.[35]

Here we propose an alternative scheme that does not require UHF calculations: valence

and core ionized states are generated as restricted excitations into a very diffuse orbital.[37,38] The emission energies are then computed as difference between the core-ionized state (c) and the valence-ionized state (v) ionization potentials, $(\mathrm{IP}_c - \mathrm{IP}_v)$. The intensities are finally computed as oscillator strengths f_{vc} between the core and valence ionized states, $f_{vc} = \frac{2}{3}(\mathrm{IP}_c - \mathrm{IP}_v)(S^{vc}_{XX} + S^{vc}_{YY} + S^{vc}_{ZZ})$, using the regular CC expressions for the transition strengths $S^{vc}_{\alpha\alpha}$ between two excited states.[17] In the EOM-CC framework, the transition moments T^{XX}_{vc} (in the notation of Ref. 17) entering the transition strength S^{vc}_{XX} are simply

$$ {}^{\mathrm{EOM}}T^{XX}_{vc} = (L_v\, {}^{\mathrm{EOM}}\mathbf{A}^X R_c) - (\bar{t} \cdot R_c)(L_v \cdot \xi^X) - (L_v \mathbf{I} R_c)(\bar{t} \cdot \xi^X) \tag{24} $$

and similarly for the other terms required.

2.3 The complex response amplitudes and multipliers

As anticipated in the previous sections, to compute the KHD scattering amplitudes we need to solve right and left complex linear equations like, e.g.,

$$ (\mathbf{A} - (\omega + i\gamma)\mathbf{I}) t^X(\omega + i\gamma) = -\xi^X \tag{25} $$

$$ \bar{t}^X(\omega' - i\gamma)(\mathbf{A} + (\omega' - i\gamma)\mathbf{I}) = -\eta^X - \mathbf{F} t^X(\omega' - i\gamma) \tag{26} $$

In the present study we adopt the algorithm presented in Ref. 32 and rewrite, e.g., the right complex equation above as

$$ \begin{cases} (\mathbf{A} - \omega\mathbf{I}) t^X_{\Re}(\tilde{\omega}) = -\xi^X_{\Re} - \gamma t^X_{\Im}(\tilde{\omega}) \\ i(\mathbf{A} - \omega\mathbf{I}) t^X_{\Im}(\tilde{\omega}) = -i\xi^X_{\Im} + i\gamma t^X_{\Re}(\tilde{\omega}) \end{cases} \tag{27} $$

where $\tilde{t}^X = t^X_{\Re} + i t^X_{\Im}$ and $\tilde{\xi}^X = \xi^X_{\Re} + i\xi^X_{\Im} \equiv \xi^X_{\Re}$, which is then recast in (pseudo-symmetric)

matrix form

$$\begin{pmatrix} (\mathbf{A}-\omega\mathbf{I}) & \gamma\mathbf{I} \\ \gamma\mathbf{I} & -(\mathbf{A}-\omega\mathbf{I}) \end{pmatrix} \begin{pmatrix} t^X_{\Re} \\ t^X_{\Im} \end{pmatrix} = \begin{pmatrix} -\xi^X_{\Re} \\ \xi^X_{\Im} \end{pmatrix} \tag{28}$$

The solution to Eq. (28) is obtained using an iterative subspace algorithm.[32] After iteration n, we have k real orthonormal trial vectors (where $k \leq 2n$)

$$\boldsymbol{b}^k = \{b_{\Re 1}, b_{\Im 1}, b_{\Re 2}, b_{\Im 2}, \ldots, b_{\Re n}, b_{\Im n}\} \tag{29}$$

$$= \{b_1, b_2, b_3, b_4, \ldots, b_{k-1}, b_k\} \tag{30}$$

and k linear transformed vectors

$$\boldsymbol{\sigma}^k = \{\mathbf{A}b_{\Re 1}, \mathbf{A}b_{\Im 1}, \mathbf{A}b_{\Re 2}, \mathbf{A}b_{\Im 2}, \ldots, \mathbf{A}b_{\Re n}, \mathbf{A}b_{\Im n}\} \tag{31}$$

$$= \{\mathbf{A}b_1, \mathbf{A}b_2, \mathbf{A}b_3, \mathbf{A}b_4, \ldots, \mathbf{A}b_{k-1}, \mathbf{A}b_k\} \tag{32}$$

A reduced response equation is set up in the subspace $\boldsymbol{b}^k$ in (30), giving

$$\begin{pmatrix} \mathbf{A}^{\mathrm{red}}-\omega\mathbf{I}^{\mathrm{red}} & \gamma\mathbf{I}^{\mathrm{red}} \\ \gamma\mathbf{I}^{\mathrm{red}} & -(\mathbf{A}^{\mathrm{red}}-\omega\mathbf{I}^{\mathrm{red}}) \end{pmatrix} \begin{pmatrix} \alpha^X_{\Re} \\ \alpha^X_{\Im} \end{pmatrix} = \begin{pmatrix} -\xi^{X,\mathrm{red}}_{\Re} \\ \xi^{X,\mathrm{red}}_{\Im} \end{pmatrix}, \tag{33}$$

where

$$\xi^{X,\mathrm{red}}_{\Re,i} = b_i^T \xi^X_{\Re}, \quad \xi^{X,\mathrm{red}}_{\Im,i} = b_i^T \xi^X_{\Im} \tag{34}$$

$$\mathbf{A}^{\mathrm{red}}_{ij} = b_i^T \sigma_j = b_i^T \mathbf{A} b_j \tag{35}$$

Index i in Eq. (34) refers to the indices of $\boldsymbol{b}^k$ in Eq. (30). The dimension of reduced space response matrix in Eq. (33) is $2k \times 2k$, due to the fact that each block has a dimension $k \times k$. Indices i and j in Eq. (35) refer to the indices of $\boldsymbol{b}^k$ in Eq. (30) and $\boldsymbol{\sigma}^k$ in Eq. (32), respectively. Due to the fact that trial vectors are orthonormal, $\mathbf{I}^{\mathrm{red}}$ is a unity matrix of

dimension $k \times k$.

Solving Eq. (33) leads to the optimal solution vectors (real and imaginary component) given as

$$t^X_{\Re,n+1} = \sum_{i=1}^{k} (\alpha^X_{\Re})_i b_i \,, \quad t^X_{\Im,n+1} = \sum_{i=1}^{k} (\alpha^X_{\Im})_i b_i \,. \tag{36}$$

The residuals $R^X_{\Re,n+1}$ and $R^X_{\Im,n+1}$ may be calculated as

$$R^X_{\Re,n+1} = (\mathbf{A} - \omega\mathbf{I}) t^X_{\Re,n+1} + \gamma \mathbf{I} t^X_{\Im,n+1} + \xi^X_{\Re} \tag{37}$$

$$= \sum_{i=1}^{k} (\alpha^X_{\Re})_i \sigma_i - \omega \sum_{i=1}^{k} (\alpha^X_{\Re})_i b_i + \gamma \sum_{i=1}^{k} (\alpha^X_{\Im})_i b_i + \xi^X_{\Re} \,, \tag{38}$$

$$R^X_{\Im,n+1} = -(\mathbf{A} - \omega\mathbf{I}) t^X_{\Im,n+1} + \gamma \mathbf{I} t^X_{\Re,n+1} - \xi^X_{\Im} \tag{39}$$

$$= -\sum_{i=1}^{k} (\alpha^X_{\Im})_i \sigma_i + \omega \sum_{i=1}^{k} (\alpha^X_{\Im})_i b_i + \gamma \sum_{i=1}^{k} (\alpha^X_{\Re})_i b_i - \xi^X_{\Im} \,, \tag{40}$$

respectively. Residuals are used to check for convergence and may be used to obtain new trial vectors according to a general equation of the form

$$\widetilde{b_{n+1}} = \mathcal{P} \widetilde{R_{n+1}} \tag{41}$$

where $\widetilde{b_{n+1}}$ is a general new trial vector, $\widetilde{R_{n+1}}$ is a general residual in iteration n+1 and $\mathcal{P}$ is a preconditioner.

Eq. (41) may be written as

$$b_{\Re,n+1} + i b_{\Im,n+1} = \mathcal{P}(R_{\Re,n+1} + i R_{\Im,n+1}) \tag{42}$$

In our case, Eq. (41) may be written as

$$\begin{pmatrix} b_{\Re,n+1} \\ b_{\Im,n+1} \end{pmatrix} = \begin{pmatrix} (\mathbf{A}_0 - \omega\mathbf{I}) & \gamma\mathbf{I} \\ \gamma\mathbf{I} & -(\mathbf{A}_0 - \omega\mathbf{I}) \end{pmatrix}^{-1} \begin{pmatrix} R_{\Re,n+1} \\ R_{\Im,n+1} \end{pmatrix} , \tag{43}$$

where $\mathbf{A}_0$ contains the diagonal elements of $\mathbf{A}$. Eq. (43) is equivalent to

$$\begin{pmatrix} b_{\Re,n+1} \\ b_{\Im,n+1} \end{pmatrix} = [(\mathbf{A}_0 - \omega\mathbf{I})^2 + \gamma^2\mathbf{I}]^{-1} \otimes \begin{pmatrix} (\mathbf{A}_0 - \omega\mathbf{I}) & \gamma\mathbf{I} \\ \gamma\mathbf{I} & -(\mathbf{A}_0 - \omega\mathbf{I}) \end{pmatrix} \begin{pmatrix} R_{\Re,n+1} \\ R_{\Im,n+1} \end{pmatrix} . \tag{44}$$

More specifically, the elements of the new trial vectors are

$$(b_{\Re,n+1})_j = \frac{A_{jj} - \omega}{(A_{jj} - \omega)^2 + \gamma^2}(R_{\Re,n+1})_j + \frac{\gamma}{(A_{jj} - \omega)^2 + \gamma^2}(R_{\Im,n+1})_j \tag{45}$$

$$(b_{\Im,n+1})_j = -\frac{A_{jj} - \omega}{(A_{jj} - \omega)^2 + \gamma^2}(R_{\Im,n+1})_j + \frac{\gamma}{(A_{jj} - \omega)^2 + \gamma^2}(R_{\Re,n+1})_j \tag{46}$$

The new trial vectors $b_{\Re,n+1}$ and $b_{\Im,n+1}$ are then added to the subspace $\boldsymbol{b}^k$ in Eq. (30) as b_{k+1} and b_{k+2} and the iteration procedure is continued until convergence is obtained.

In the right complex equations, Eq. 25, the right-hand-side vectors are generally either purely real (for real operators) or purely imaginary (for imaginary operators). In the right-hand-side of the left complex equation, Eq. 26, on the other hand, there are always both imaginary and real components, due to the presence of the complex amplitudes.

3 Computational details

The same geometry as used in Ref. 12 was adopted for water. Symmetry labels throughout are relative to the molecule placed on the yz axis, with z as C_2 axis. The protocols described in the previous section for both the RIXS amplitudes and the CPP solver were implemented in python as a stand-alone code[39] interfaced to Psi4.[40] Pople's 6-311++G** basis set in its pure (spherical) form was adopted for the calculations, further supplemented with a set of

s and p Rydberg-type functions placed on the oxygen atom (with quantum numbers $n = 3$, 3.5, 4).[41]

The spectral slices of the RIXS map were generated by calculating the scattering cross-sections $\sigma^{0f}_{45^\circ}(\omega)$ of each of the first twenty valence excited states at the given incident energy, and subsequently broadening with a Lorentzian lineshape function, using the broadening parameter $\gamma = 0.124$ eV, as also used in the ADC study of Ref. 12. The same broadening factor was also applied to the non-resonant spectrum, where only a couple of valence ionized states needed to be treated in order to cover the spectral region shown in the next section.

4 Results and discussion

We report in Table 1 the excitation energies and strengths for the first 12 valence excitations (including the dipole forbidden ones), the first four dipole allowed core excitations, and the emission energies from the core ionized state to the first three valence ionized states obtained at the CCSD level in the 6-311++G**+Rydberg basis set. All core-related values were obtained without imposing any core-valence separation.[42] The 1 $^1B_1$, 1 $^1A_2$, 2 $^1A_1$ and 1 $^1B_2$ states (*vide infra*) are the main contributors to the RIXS transitions, and their position is quite well reproduced at the chosen level of theory compared to existing experimental data.[43–47] The intensity of the first excitation is also in very good agreement with the experimentally derived one,[44] whereas the intensity of the 2 $^1A_1$ excitation is overestimated.

Table 1: H_2O. Computed spectral parameters at the CCSD/6-311++G**+Rydberg level: excitation energies (E), transition strengths (S) and oscillator strength (f) of UV (VUV) and X-ray (XAS) absorption; Non-resonant emission energies and intensities (XES); Resonant Inelastic X-ray Scattering main contributors' positions (RIXS). Symmetry labels are relative to the molecule placed on the yz axis, with z as C_2 axis.

	Exc.state	E/eV	S/a.u	f	E^{expt}/eV	f^{expt}
VUV	$1\ ^1B_1\ (x)$	7.407	0.2588	0.04697	7.45[a]	0.046[b]
	$1\ ^1A_2\ (-)$	9.155	0.0	0.0	9.1[c]	
	$2\ ^1A_1\ (z)$	9.742	0.362	0.0863	9.99[a]	0.05[d]
	$2\ ^1B_1\ (x)$	10.01	0.0204	0.00499		
	$3\ ^1A_1\ (z)$	10.10	0.0537	0.01328		
	$3\ ^1B_1\ (x)$	10.39	0.00132	0.00034		
	$2\ ^1A_2\ (-)$	10.80	0.0	0.0		
	$4\ ^1B_1\ (x)$	11.21	0.00461	0.00127		
	$4\ ^1A_1\ (z)$	11.22	0.00016	0.00004		
	$5\ ^1B_1\ (x)$	11.30	0.00055	0.00015		
	$3\ ^1A_2\ (-)$	11.43	0.0	0.0		
	$1\ ^1B_2\ (y)$	11.50	0.08191	0.02308	11.5[e]	
XAS	$1s \rightarrow 4a_1$	535.74	0.0009	0.0124 (1.0)	534.0[f]	(1.0)
	$1s \rightarrow 2b_2$	537.53	0.0020	0.0258 (2.0)	535.9[f]	(1.3)
	$1s \rightarrow 2b_1$	538.93	0.0004	0.0058	537.1[f]	
	$1s \rightarrow 5a_1$	539.03	0.0003	0.0044		
	Emission line					
XES						
$1s \rightarrow \infty$	$1b_1^{-1}$	529.15	0.0043	0.0554	527.1[g]	
	$3a_1^{-1}$	526.92	0.0035	0.0453	525.4[g]	
	$1b_2^{-1}$	522.51	0.0031	0.0398	521.0[g]	
RIXS						
$1s \rightarrow 4a_1$	$1b_1^{-1}$	528.3			$\approx$526.2[g]	
	$3a_1^{-1}$	526.0			$\approx$524.2[g]	
$1s \rightarrow 2b_2$	$1b_1^{-1}$				$\approx$526.8[g]	
	$3a_1^{-1}$				$\approx$524.5[g]	

[a]From Ref. 43; [b]From Ref. 44; [c]From Ref. 45; [d]From Ref. 46; [e]From Ref. 47; [f]From Ref. 48; [g]From Ref. 4.

In the chosen basis set, and as previously observed,[49,50] the first two core excitation energies are systematically overestimated at the CCSD level, respectively by 1.74 eV and 1.67 eV, compared to the experimental peak maxima. This results in a slightly smaller

separation between the two computed XAS peaks (1.79 eV) than the separation between the experimental peaks (1.9 eV). The relative intensities of the first two excitations are also slightly overestimated compared to the experimentally derived (relative) strengths. The intensity ratio determined is equivalent to the one reported at the ADC(2)-x and ADC(3/2) level in Ref. 12.

Turning to the non-resonant XES, the position of our $1b_1^{-1}$ emission line is ≈2 eV higher than in the experimental case, whereas the other two lines are ≈1.5 eV higher. We will return to the discussion of the emission intensities later on.

On Table 2, we have summarized the cross-section values obtained for the states that contribute most to the RIXS spectral slices. We report both CCSD and EOM-CCSD results obtained using two different basis sets, namely the standard 6-311++G** set and the 6-311++G** set supplemented with Rydberg functions. They are compared with the corresponding ADC results from Ref. 12.

Table 2: H_2O. RIXS transition strengths $\sigma^{0f}_{45^\circ}$ calculated at the resonance frequency of the two lowest core-excited states.[c]

	Resonance ($1s \rightarrow 4a_1$)		Resonance ($1s \rightarrow 2b_1$)	
Method	1^1B_1	2^1A_1	1^1A_2	1^1B_2
CCSD/[a]	0.021 (1.56)	0.014	0.043 (1.28)	0.033
CCSD/[b]	0.021 (1.81)	0.012	0.041 (1.30)	0.032
EOM-CCSD/[a]	0.021 (1.55)	0.013	0.042 (1.28)	0.033
EOM-CCSD/[b]	0.021 (1.82)	0.011	0.040 (1.30)	0.031
ADC(2)/[a]	0.012 (1.47)	0.008	0.019 (1.23)	0.016
ADC(2)-x/[a]	0.016 (1.51)	0.011	0.031 (1.26)	0.025
ADC(3/2)/[a]	0.027 (1.57)	0.017	0.053 (1.34)	0.040
Expt.	(1.7±0.2)	(1.0)	(1.2±0.2)	(1.0)

[a] 6-311++G** ;
[b] 6-311++G** + Rydberg($n = 3, 3.5, 4$)
[c] Transition strengths normalized to the σ value of the second final state are given in parenthesis. Experimental data are from Ref. 4; ADC results are from Ref. 12.

Inspection of the results in Table 2 shows that quadratic response (QR) CCSD and EOM-CCSD yield almost identical results for the RIXS cross sections. Addition of the Rydberg functions slightly reduces the intensity of the 2 $^1A_1$ state at the first resonance, increasing

hereby the relative intensity of the emission line at higher energy (1^1B_1), in agreement with experiment. It should be noticed, nonetheless, that both basis sets yield relative cross-section intensity values that accommodate within the experimental error bars. At both resonances, the QR-CCSD/EOM-CCSD cross-sections are in-between the ADC(2)-x and the ADC(3/2) ones, which were obtained in Ref. 12 in the 6-311++G** basis set without Rydberg type functions. The authors of Ref. 12 do not report the numerical value of the peak maxima in the RIXS spectrum, but indicative values can be inferred from an inspection of Fig. 1 in Ref. 12. For ADC(3/2), the 1^1B_1 maximum is at around 531.1 eV and the 2^1A_1 one at around 528.7 eV ($4a_1$ resonance); the 1^1A_2 maximum is at around 530.9 eV and the 2^1B_2 one at around 528.5 eV ($2b_2$ resonance). The deviations from the experimental peak maxima are thus of the order of 5 eV. Our CCSD maxima, on the other hand, see Table 2, are off the experimental ones by roughly 2 eV.

RIXS spectral slices are shown on the top panel of Fig. 1, together with the non-resonant XES spectrum for the QR-CCSD case in the larger basis set. Only the first two bands are included in both cases. The EOM slices are shown on the left panel at the bottom and are basically identical to the QR-CCSD ones. A so-called RIXS map is shown on the right. Comparing the RIXS slices with the experimental ones shown in Fig. 3 of Ref. 4, we observe the same general trends as in experiment: the emission peaks shift to higher energy when changing the resonance excitation energy, including the non-resonant case. Notice that the third emission peak was not included in our calculated RIXS and non-resonant XES spectra in Fig. 1. Fig. 1 also shows that even if the decay into the four above mentioned valence excited states yield most of the emission intensities, other states are also contributing. The arrows in the spectra in the top panel indicate that different states are probed at different incident frequencies. For the spectrum at 538.98 eV, the incident light was chosen in near resonance with two very close lying core excited states, and one can clearly see that two valence states are the main contributors to the intense bands at this incident frequency.

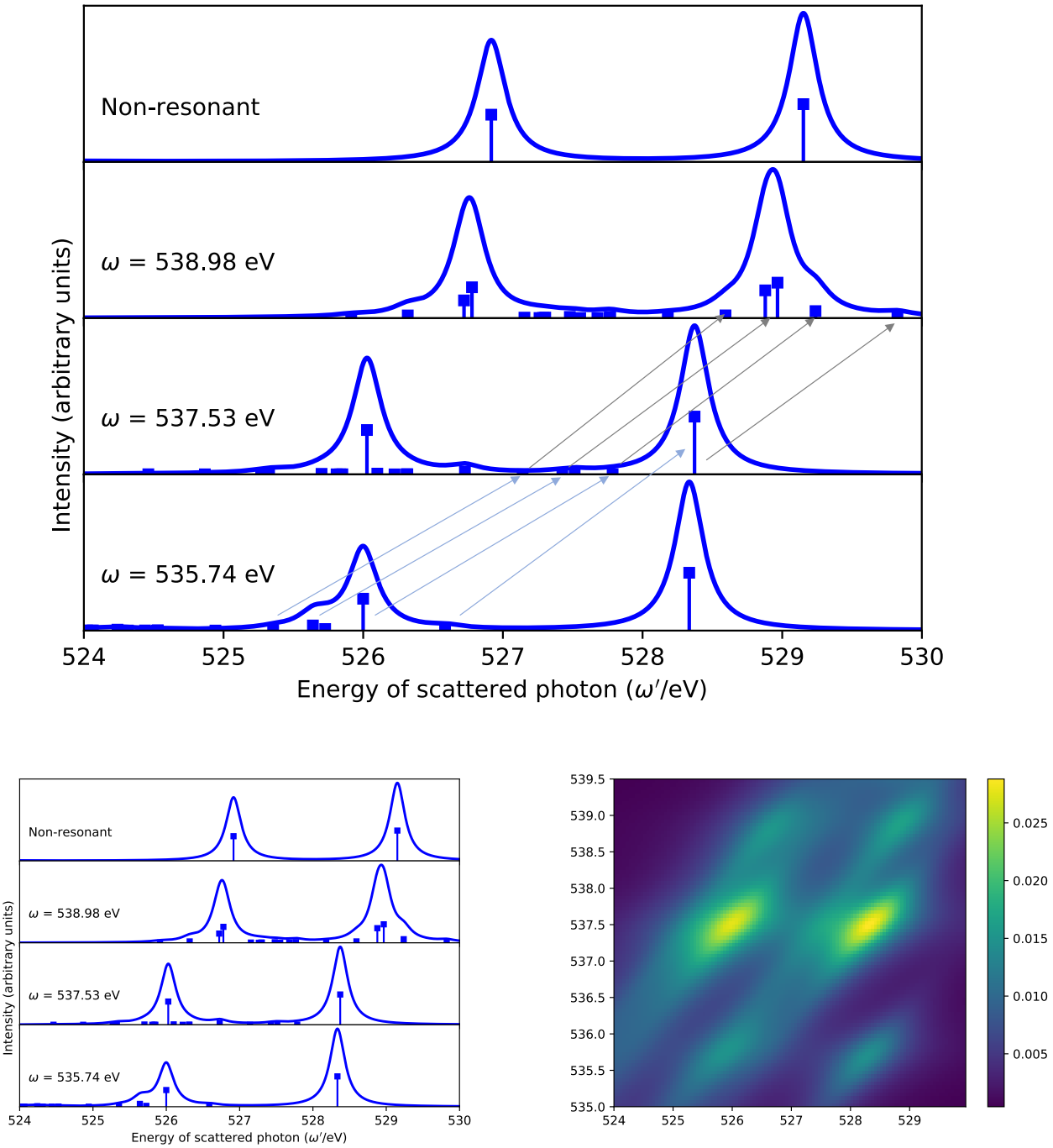

Figure 1: Top: Slices of the core emission spectrum, when the incident beam is at resonance with each of the first few core excited states (RIXS) and when a beam frequency beyond the ionization threshold is used (XES, labeled "Non-resonant"). QR-CCSD/6-311^{++}G** + (3s,3p)–Rydberg(n=3, 3.5, 4) results. The arrows highlight how different states are probed at different resonant frequencies. Bottom left: EOM-CCSD slices of the core emission spectrum. Right: RIXS map, QR-CCSD/6-311^{++}G** + (3s,3p)–Rydberg(n=3, 3.5, 4).

5 Conclusions

A computational expression for the Kramers−Heisenberg−Dirac scattering amplitude of resonant inelastic X-ray scattering (RIXS) has been derived in the framework of damped coupled cluster and equation-of-motion coupled cluster quadratic response theory, and implemented at the coupled cluster singles and doubles level. A practical recipe to obtain non-resonant x-ray emission spectra (XES) at the same levels of theory that does not require unrestricted Hartree-Fock calculations has also been proposed. This further extend the applicability of the highly successful and rather accurate coupled cluster response methodologies within of realm of x-ray spectroscopy.

As illustrative case study, we have considered the water molecule in gas phase, for which accurate experimental RIXS data,[4] as well as very recent ADC results obtained with a similar strategy,[12] are available. Very good agreement with the experimental data was obtained. Moreover, no significant difference was observed between the results obtained from "standard" quadratic response and those obtained from the computationally simpler equation-of-motion expressions.

6 Appendix: alternative derivation of the EOM-CC KHD amplitudes

As noted in an earlier section, the EOM-CC approach can and has traditionally be derived by treating the biorthogonal eigenvectors of an effective Hamiltonian constructed by projecting the similarity transformed Hamiltonian, $\exp(-T)\hat{H}\exp(T)$, into a complete set determinants.[18] Due to fact that the amplitudes have solved to satisfy the CC equations, this effective Hamiltonian takes the simple form

$$(\bar{H} - E_{CC}) = \begin{pmatrix} 0 & \eta \\ 0 & \mathbf{A} \end{pmatrix}. \tag{47}$$

The ground-state left and right eigenvectors are found as $\tilde{L}_0 = (1, \bar{t})$ and $\tilde{R}_0 = (1, 0)$, with an eigenvalue of 0, in correspondence with normal CC theory. Similarly, eigenvectors corresponding to excited states are $\tilde{L}_n = (0, L_n)$ and $\tilde{R}_n = (-\bar{t} \cdot R_n, R_n)$, where L_n, R_n and the eigenvalues ω_n are identical to the results of CC response theory. In EOM-CC, these vectors are then interpreted as states, such that

$$|\Psi_0^{\mathrm{EOM}}\rangle = \exp(T)|\mathrm{HF}\rangle \tag{48}$$

$$|\Psi_n^{\mathrm{EOM}}\rangle = (\bar{t} \cdot R_n + \sum_{\mu} R_{\mu,n}\tau_\mu) \exp(T)|\mathrm{HF}\rangle \tag{49}$$

$$\langle\Psi_0^{\mathrm{EOM}}| = \langle\Lambda| \tag{50}$$

$$\langle\Psi_n^{\mathrm{EOM}}| = \sum_{\mu} L_{\mu,n}\langle\mu| \exp(-T) \tag{51}$$

The relevant moments then become:

$$\langle\Psi_n^{\mathrm{EOM}}|\hat{X}|\Psi_0^{\mathrm{EOM}}\rangle = L_n \cdot \xi^X \tag{52}$$

$$\langle\Psi_0^{\mathrm{EOM}}|\hat{X}|\Psi_n^{\mathrm{EOM}}\rangle = {}^{\mathrm{EOM}}\eta^X \cdot R_n \tag{53}$$

$$\langle\Psi_n^{\mathrm{EOM}}|\bar{X}|\Psi_m^{\mathrm{EOM}}\rangle = L_n {}^{\mathrm{EOM}}\mathbf{A}^X R_m - (\bar{t} \cdot \xi^X)(L_n \cdot R_m) - (L_n \cdot \xi^X)(\bar{t} \cdot R_m) \tag{54}$$

We can then write the right KHD amplitude as

$$\begin{aligned} {}^{\mathrm{EOM-CC}}\mathcal{F}_{XY}^{f0}(\omega) = &\sum_{n>0} \frac{\left[L_f {}^{\mathrm{EOM}}\mathbf{A}^X R_n - (\bar{t} \cdot \xi^X)(L_f \cdot R_n) - (L_f \cdot \xi^X)(\bar{t} \cdot R_n)\right] L_n \cdot \xi^Y}{\omega_n - (\omega + i\gamma)} \\ &+ \sum_{n>0} \frac{\left[L_f {}^{\mathrm{EOM}}\mathbf{A}^Y R_n - (\bar{t} \cdot \xi^Y)(L_f \cdot R_n) - (L_f \cdot \xi^Y)(\bar{t} \cdot R_n)\right] L_n \cdot \xi^X}{\omega_n + (\omega' + i\gamma)} \end{aligned} \tag{55}$$

Using the full set of eigenvectors, is possible to rewrite Eq. (8) as

$$t^Y(\omega + i\gamma) = -\sum_{n>0} \frac{R_n(L_n \cdot \xi^Y)}{\omega_n - (\omega + i\gamma)} \tag{56}$$

using which, Eq. (55) can easily be seen to be identical to Eq. (19). Similarly, the left amplitude can be written

$$
\begin{aligned}
{}^{\mathrm{EOM-CC}}\mathcal{F}^{0f}_{XY}(\omega) = &\sum_{n>0} \frac{({}^{\mathrm{EOM}}\eta^{Y} \cdot R_n)\left[L_n {}^{\mathrm{EOM}}\mathbf{A}^{X} R_f - (\bar{t}\cdot\xi^{X})(L_n\cdot R_f) - (L_n\cdot\xi^{X})(\bar{t}\cdot R_f)\right]}{\omega_f - (\omega - i\gamma)} \\
&+ \sum_{n>0} \frac{({}^{\mathrm{EOM}}\eta^{X} \cdot R_n)\left[L_n {}^{\mathrm{EOM}}\mathbf{A}^{Y} R_f - (\bar{t}\cdot\xi^{Y})(L_n\cdot R_f) - (L_n\cdot\xi^{Y})(\bar{t}\cdot R_f)\right]}{\omega_n + (\omega' - i\gamma)}
\end{aligned}
\tag{57}
$$

which again can be rewritten as Eq. (21) by using the spectral form of Eq. (17).

Acknowledgement

The authors acknowledge financial support from DTU Chemistry and from the Independent Research Fund Denmark - DFF-Forskningsprojekt2 grant no. 7014-00258B. S.C. acknowledges support from the Otto Mønsteds Fund for a travel grant to present this work at the 256th Americal Chemical Society National Meeting and Exposition in Boston, US.

References

(1) Gel'mukhanov, F.; Ågren, H. Resonant X-ray Raman Scattering. *Phys. Rep.* **1999**, *312*, 87–330.

(2) Carra, P.; Fabrizio, M.; Thole, B. T. High Resolution X-Ray Resonant Raman Scattering. *Phys. Rev. Lett.* **1995**, *74*, 3700–3703.

(3) Baker, M. L.; Mara, M. W.; Yan, J. J.; Hodgson, K. O.; Hedman, B.; Solomon, E. I. K- and L-edge X-ray Absorption Spectroscopy (XAS) and Resonant Inelastic X-ray Scattering (RIXS) Determination of Differential Orbital Covalency (DOC) of Transition Metal Sites. *Coord. Chem. Rev.* **2017**, *345*, 182–208.

(4) Weinhardt, L.; Benkert, A.; Meyer, F.; Blum, M.; Wilks, R. G.; Yang, W.; Bär, M.;

Reinert, F.; Heske, C. Nuclear dynamics and spectator effects in resonant inelastic soft x-ray scattering of gas-phase water molecules. *J. Chem. Phys.* **2012**, *136*, 144311.

(5) Benkert, A.; Meyer, F.; Hauschild, D.; Blum, M.; Yang, W.; Wilks, R. G.; Baer, M.; Reinert, F.; Heske, C.; Weinhardt, L. Isotope Effects in the Resonant Inelastic Soft X-ray Scattering Maps of Gas-Phase Methanol. *J. Phys. Chem. A* **2016**, *120*, 2260–2267.

(6) Gejo, T.; Oura, M.; Tokushima, T.; Horikawa, Y.; Arai, H.; Shin, S.; Kimberg, V.; Kosugi, N. Resonant inelastic x-ray scattering and photoemission measurement of O_2: Direct evidence for dependence of Rydberg-valence mixing on vibrational states in O 1s $\rightarrow$ Rydberg states. *J. Chem. Phys.* **2017**, *147*, 044310.

(7) Weinhardt, L.; Ertan, E.; Iannuzzi, M.; Weigand, M.; Fuchs, O.; Bär, M.; Blum, M.; Denlinger, J. D.; Yang, W.; Umbach, E.; Odelius, M.; Heske, C. Probing hydrogen bonding orbitals: resonant inelastic soft X-ray scattering of aqueous NH_3. *Phys. Chem. Chem. Phys.* **2015**, *17*, 27145–27153.

(8) Liu, Y.-S.; Glans, P.-A.; Chuang, C.-H.; Kapilashrami, M.; Guo, J. Perspectives of in situ/operando resonant inelastic X-ray scattering in catalytic energy materials science. *J Electron Spectros. Relat. Phenomena.* **2015**, *200*, 282–292.

(9) Kunnus, K.; Zhang, W.; Delcey, M. G.; Pinjari, R. V.; Miedema, P. S.; Schreck, S.; Quevedo, W.; Schröder, H.; Fölisch, A.; Gaffney, K. J.; Lundberg, M.; Odelius, M.; Wernet, P. Viewing the Valence Electronic Structure of Ferric and Ferrous Hexacyanide in Solution from the Fe and Cyanide Perspectives. *J. Phys. Chem. B* **2016**, *120*, 7182–7194.

(10) Long, D. A. *The Raman Effect: A Unified Treatment of the Theory of Raman Scattering by Molecules*; John Wiley & Sons Ltd., 2002.

(11) Rehn, D. R.; Dreuw, A.; Norman, P. Resonant inelastic X-ray scattering amplitudes in the ADC/ISR framework. Pisa, April 10-12, 2017; Abstract of contributed talk at the

conference "MPCS17 - Molecular Properties and Computational Spectroscopy - From Esoteric Effects to Novel Spectroscopic Probes".

(12) Rehn, D. R.; Dreuw, A.; Norman, P. Resonant inelastic X-ray scattering amplitudes and cross-sections in the algebraic diagrammatic construction/intermediate state representation (ADC/ISR) approach. *J. Chem. Theory Comput.* **2017**, *13*, 5552–5559.

(13) Schirmer, J. Beyond the random-phase approximation: A new approximation scheme for the polarization propagator. *Phys. Rev. A* **1982**, *26*, 2395–2416.

(14) Schirmer, J.; Trofimov, A. B. Intermediate state representation approach to physical properties of electronically excited molecules. *J. Chem. Phys.* **2004**, *120*, 11449–11464.

(15) Dreuw, A.; Wormit, M. The algebraic diagrammatic construction scheme for the polarization propagator for the calculation of excited states. *WIREs Comput Mol Sci* **2015**, *5*, 82–95.

(16) Koch, H.; Jørgensen, P. Coupled Cluster Response Functions. *J. Chem. Phys.* **1990**, *93*, 3333–3344.

(17) Christiansen, O.; Jørgensen, P.; Hättig, C. Response Functions from Fourier Component Variational Perturbation Theory Applied to a Time-Averaged Quasienergy. *Int. J. Quantum Chem.* **1998**, *98*, 1.

(18) Stanton, J. F.; Bartlett, R. J. The equation of motion coupled-cluster method. A systematic biorthogonal approach to molecular excitation energies, transition probabilities, and excited state properties. *J. Chem. Phys.* **1993**, *98*, 7029–7039.

(19) Krylov, A. I. Equation-of-Motion Coupled-Cluster Methods for Open-Shell and Electronically Excited Species: The Hitchhiker's Guide to Fock Space. *Ann. Rev. Phys. Chem.* **2008**, *59*, 433–462.

(20) Bartlett, R. J. Coupled-cluster theory and its equation-of-motion extensions. *WIREs Comput. Mol. Sci. 2*, 126–138.

(21) Weisskopf, V.; Wigner, E. Berechnung der natürlichen Linienbreite auf Grund der Dirac schen Lichttheorie. *Z. Phys.* **1930**, *63*, 54–73.

(22) Weisskopf, V.; Wigner, E. Über die natürliche Linienbreite in der Strahlung des harmonischen Oszillators. *Z. Phys.* **1930**, *65*, 18–29.

(23) Buckingham, A.; Fisher, P. Phenomenological damping in optical response tensors. *Phys. Rev. A.* **2000**, *61*, 035801.

(24) Norman, P.; Bishop, D. M.; Jensen, H. J. A.; Oddershede, J. Nonlinear response theory with relaxation: The first-order hyperpolarizability. *J. Chem. Phys.* **2005**, *123*, 194103.

(25) Norman, P. A perspective on non resonant and resonant electronic response theory for time-dependent molecular properties. *Phys. Chem. Chem. Phys.* **2011**, *12*, 20519–20535.

(26) Norman, P.; Bishop, D.; Jø"rgen, H.; Jensen, A.; Oddershede, J. Near-resonant absorption in the time-dependent self-consistent field and multiconfigurational self-consistent field approximations. *Chem. Phys.* **2001**, *10323*.

(27) Kristensen, K.; Kauczor, J.; Kjaergaard, T.; Jørgensen, P. Quasienergy formulation of damped response theory. *J. Chem. Phys.* **2009**, *131*, 044112.

(28) Göppert-Mayer, M. Über Elementarakte mit zwei Quantensprüngen. *Ann. Phys. (Leipzig)* **1931**, *9*, 273–294.

(29) Swofford, R. L.; Vricht, A. C. A. Nonlinear Spectroscopy. *Annu. Rev. Phys. Chem.* **1978**, *29*, 421–440.

(30) Olsen, J.; Jørgensen, P. Linear and non-linear response functions for an exact state and for an MCSCF state. *J. Chem. Phys.* **1985**, *82*, 3235–3264.

(31) Helgaker, T.; Coriani, S.; Jørgensen, P.; Kristiansen, K.; Olsen, J.; Ruud, K. Recent Advances in Wave Function Based Methods of Molecular-Property Calculations. *Chem. Rev.* **2012**, *112*, 543–631.

(32) Kauczor, J.; Norman, P.; Christiansen, O.; Coriani, S. Communication: A reduced-space algorithm for the solution of the complex linear response equations used in coupled cluster damped response theory. *J. Chem. Phys.* **2013**, *139*, 211102.

(33) Coriani, S.; Pawlowski, F.; Olsen, J.; Jørgensen, P. Molecular response properties in equation of motion coupled cluster theory: A time-dependent perspective. *J. Chem. Phys.* **2016**, *144*, 024102.

(34) Pawlowski, F.; Olsen, J.; Jørgensen, P. Molecular response properties from a Hermitian eigenvalue equation for a time-periodic Hamiltonian. *J. Chem. Phys.* **2015**, *142*, 114109.

(35) Besley, N. A. Equation of motion coupled cluster theory calculations of the X-ray emission spectroscopy of water. *Chem. Phys. Lett.* **2012**, *542*, 42–46.

(36) Gilbert, A. T. B.; Besley, N. A.; Gill, P. M. W. Self-Consistent Field Calculations of Excited States Using the Maximum Overlap Method (MOM). *J. Phys. Chem. A* **2008**, *112*, 13164–13171.

(37) Stanton, J.; Gauss, J. A simple scheme for the direct calculation of ionization potentials with coupled-cluster theory that exploits established excitation energy methods. *J. Chem. Phys.* **1999**, *111*, 8785.

(38) Coriani, S.; Koch, H. X-ray absorption spectra and core-ionization potentials within a core-valence separated coupled-cluster framework. *J. Chem. Phys.* **2015**, *143*, 181103.

(39) Faber, R. 2018; Python module `response_solver_experiments`.

(40) Parrish, R. M.; Burns, L. A.; Smith, D. G. A.; Simmonett, A. C.; DePrince, A. E.; Hohenstein, E. G.; Bozkaya, U.; Sokolov, A. Y.; Di Remigio, R.; Richard, R. M.;

Gonthier, J. F.; James, A. M.; McAlexander, H. R.; Kumar, A.; Saitow, M.; Wang, X.; Pritchard, B. P.; Verma, P.; Schaefer, H. F.; Patkowski, K.; King, R. A.; Valeev, E. F.; Evangelista, F. A.; Turney, J. M.; Crawford, T. D.; Sherrill, C. D. Psi4 1.1: An Open-Source Electronic Structure Program Emphasizing Automation, Advanced Libraries, and Interoperability. *J. Chem. Theory Comput.* **2017**, *13*, 3185–3197.

(41) Kaufmann, K.; Baumeister, W.; Jungen, M. Universal gaussian-basis sets for an optimum representation of Rydberg and continuum wavefunctions. *J. Phys. B – At. Mol. Opt.* **1989**, *22*, 2223–2240.

(42) Cederbaum, L. S.; Domcke, W.; Schirmer, J. Many-body theory of core holes. *Phys. Rev. A: At., Mol., Opt. Phys.* **1980**, *22*, 206−222.

(43) Mota, R.; Parafita, R.; Giuliani, A.; Hubin-Franskin, M.-J.; Lourenco, J.; Garcia, G.; Hoffmann, S.; Mason, N.; Ribeiro, P.; Raposo, M.; Limão-Vieira, P. Water VUV electronic state spectroscopy by synchrotron radiation. *Chem. Phys. Lett.* **2005**, *416*, 152–159.

(44) Thorn, P. A.; Brunger, M. J.; Teubner, P. J. O.; Diakomichalis, N.; Maddern, T.; Bolorizadeh, M. A.; Newell, W. R.; Kato, H.; Hoshino, M.; Tanaka, H.; Cho, H.; Kim, Y.-K. Cross sections and oscillator strengths for electron-impact excitation of the A ^{1}B1 electronic state of water. *J. Chem. Phys.* **2007**, *126*, 064306.

(45) Chutjian, A.; Hall, R. I.; Trajmar, S. Electron-impact excitation of H_2O and D_2O at various scattering angles and impact energies in the energy-loss range 4–212 eV. *J. Chem. Phys.* **1975**, *63*, 892–898.

(46) Wang, H. T.; Felps, W. S.; McGlynn, S. P. Molecular Rydberg states. VII. Water. *J. Chem. Phys.* **1977**, *67*, 2614–2628.

(47) Dutuit, O.; Tabche-Fouhaile, A.; Nenner, I.; Frohlich, H.; Guyon, P. M. Photodissocia-

tion processes of water vapor below and above the ionization potential. *J. Chem. Phys.* **1985**, *83*, 584–596.

(48) Schirmer, J.; Trofimov, A. B.; Randall, K. J.; Feldhaus, J.; Bradshaw, A. M.; Ma, Y.; Chen, C. T.; Sette, F. K-shell excitation of the water, ammonia, and methane molecules using high-resolution photoabsorption spectroscopy. *Phys. Rev. A: At., Mol., Opt. Phys.* **1993**, *47*, 1136–1147.

(49) Coriani, S.; Christiansen, O.; Fransson, T.; Norman, P. Coupled-cluster response theory for near-edge X-ray-absorption fine structure of atoms and molecules. *Phys. Rev. A* **2012**, *85*, 022507.

(50) Carbone, J.; Cheng, L.; Myhre, R.; Matthews, D.; Koch, H.; Coriani, S. An analysis of the performance of coupled cluster methods for core excitations and core ionizations using standard basis sets. 2018; to be submitted.